

1 Rate Dependent Performance Related to Crystal Structure Evolution 2 of Na_{0.67}Mn_{0.8}Mg_{0.2}O₂ in a Sodium-Ion Battery

3 Neeraj Sharma,^{*,†} Nuria Tapia-Ruiz,[‡] Gurpreet Singh,[§] A. Robert Armstrong,^{||} James C. Pramudita,[†]
4 Helen E. A. Brand,[⊥] Juliette Billaud,^{||} Peter G. Bruce,[‡] and Teofilo Rojo^{*,§,¶}

5 [†]School of Chemistry, UNSW Australia, Sydney, New South Wales 2052, Australia

6 [‡]Department of Materials, University of Oxford, Oxford OX1 3PH, United Kingdom

7 [§]CICenergigune, Parque Tecnológico de Álava, Albert Einstein 48, ED.CIC, 01510, Miñano, Spain

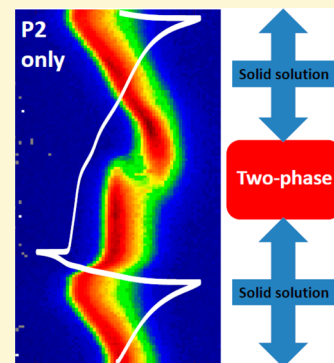
8 ^{||}School of Chemistry, University of St. Andrews, St. Andrews, Fife KY16 9ST, United Kingdom

9 [⊥]Australian Synchrotron, 800 Blackburn Road, Clayton, Melbourne, Victoria 3168, Australia

10 [¶]Departamento de Química Inorgánica, Universidad del País Vasco UPV/EHU, P.O. Box. 644, 48080, Bilbao, Spain

11 **S** Supporting Information

12 **ABSTRACT:** Sodium-ion batteries are considered as a favorable alternative to the widely
13 used lithium-ion batteries for applications such as grid-scale energy storage. However, to meet
14 the energy density and reliability that is necessary, electrodes that are structurally stable and
15 well characterized during electrochemical cycling need to be developed. Here, we report on
16 how the applied discharge current rate influences the structural evolution of
17 Na_{0.67}Mn_{0.8}Mg_{0.2}O₂ electrode materials. A combination of *ex situ* and *in situ* X-ray diffraction
18 (XRD) data were used to probe the structural transitions at the discharged state and during
19 charge/discharge. *Ex situ* data shows a two-phase electrode at the discharged state comprised
20 of phases that adopt *Cmcm* and *P6₃/mmc* symmetries at the 100 mA/g rate but a
21 predominantly *P6₃/mmc* electrode at 200 and 400 mA/g rates. *In situ* synchrotron XRD data
22 at 100 mA/g shows a solely *P6₃/mmc* electrode when 12 mA/g charge and 100 mA/g
23 discharge is used even though *ex situ* XRD data shows the presence of both *Cmcm* and *P6₃/*
24 *mmc* phases. The *in situ* data allows the Na site occupancy evolution to be determined as well
25 as the rate of lattice expansion and contraction. Electrochemically, lower applied discharge
26 currents, e.g., 100 mA/g, produce better capacity than higher applied currents, e.g., 400 mA/g, and this is related in part to the
27 quantity of the *Cmcm* phase that is formed near the discharged state during a two-phase reaction (*via ex situ* measurements), with
28 lower rates producing more of this *Cmcm* phase. Thus, producing more *Cmcm* phase allows access to higher capacities while
29 higher rates show a lower utilization of the cathode during discharge as less (if any) *Cmcm* phase is formed. Therefore, this work
30 shows how structural transitions can depend on the electrochemically applied current which has significant ramifications on how
31 sodium-ion batteries, and batteries in general, are analyzed for performance during operation.



32 ■ INTRODUCTION

33 Sodium-ion batteries (NIBs) are currently being reinvestigated
34 following their inception in 1980s¹ due to the increasing energy
35 demand and the requirement to find alternatives to Li-ion
36 storage. This requirement is further motivated by the elevated
37 price of Li as well as the relatively limited and politically
38 controlled character of Li-sources.^{2,3} Sodium-ion batteries have
39 the potential to be perfect candidates for the next generation of
40 batteries due to their high abundance (6th most abundant
41 element in Earth) and wide distribution, giving them excellent
42 economic viability. Notably, Na-ion batteries may find
43 important use in large-scale grid systems (where energy density
44 is a less prominent factor) which store energy from renewable
45 and intermittent sources such as solar and wind.

46 Currently, cathode materials for NIBs are the most actively
47 researched. Structures that form layered oxides, of the type
48 Na_yMO₂ (where M is a first-row transition metal or a
49 combination of transition metals), are shown to be promising

cathode materials for Na-ion batteries due to their high
50 reversible capacity, and for M = Fe and Mn, cost and safety.²⁻⁴
51 These materials share many common features with their Li-
52 counterparts despite the larger size of Na. Sodium layered
53 oxides are typically identified using Delmas' notation⁵ P2, P3,
54 O3, etc., where P and O indicate the Na sites (P = trigonal
55 prismatic and O = octahedral) and the number relates to the
56 transition metal layers within the unit cell. From this
57 classification, numerous studies have been reported for P2-
58 type Na_yMO₂ materials demonstrating their higher capacities,
59 diffusion rate, and better cyclability than that of the O3
60 structure.⁶

In 1999, Paulsen and Dahn reported an exhaustive study on
62 P2-sodium manganese oxide compounds⁷ after reports from
63

Received: June 7, 2015

Revised: September 27, 2015

64 Parant et al., two decades prior, first showed evidence of this
65 phase while elucidating the phase diagram of Na_xMnO_2 .⁸ Even
66 then, these authors anticipated that Li and transition metal
67 doping in $\text{P2-Na}_y\text{Mn}_x\text{M}_z\text{O}_2$ reduces the Mn^{3+} Jahn–Teller
68 distortion which in turn, increases its temperature stability
69 range. Billaud et al. more recently reported the P2-type
70 $\text{Na}_{0.67}\text{Mn}_{1-x}\text{Mg}_x\text{O}_2$ material, where $0 \leq x \leq 0.2$, exhibits a
71 capacity of 175 mA h/g with excellent capacity retention. They
72 attributed the high cycle efficiency to the Mg dopant, albeit
73 with the trade-off of less capacity (150 mA h/g for
74 $\text{Na}_{0.67}\text{Mn}_{0.8}\text{Mg}_{0.2}\text{O}_2$).⁹ Furthermore, Mg prevented $\text{Mn}^{3+}/$
75 Mn^{4+} ordering within the structure during charge/discharge
76 which was reflected in a reduction of the sharp drops of voltage
77 in the electrochemical curves. Shortly after, Yabuuchi et al.
78 reported on the performance of P2-type $\text{Na}_{2/3}\text{Mg}_{0.28}\text{Mn}_{0.72}\text{O}_2$
79 showing capacities (>200 mA h/g)¹⁰ higher than those
80 expected for the $\text{Mn}^{3+}/\text{Mn}^{4+}$ redox couple. A possible
81 explanation given for these results was a reversible oxygen
82 redox reaction, analogous to O3-type lithium-excess manganese
83 oxides.¹¹ This material, however, showed poor cyclability with a
84 drop in capacity to 150 mA h/g after just 30 cycles.

85 To our knowledge, there are few reports in the literature
86 showing enhanced fast-rate performance in sodium layered
87 cathode materials. Kim et al. reported superior rate capability
88 for $\text{Na}_{0.85}\text{Li}_{0.17}\text{Ni}_{0.21}\text{Mn}_{0.64}\text{O}_2$ (a capacity of 65 mA h g⁻¹ at a
89 rate of 25 C).¹² More recently, Komaba and co-workers
90 reported a large reversible capacity (>100 mA h/g) for
91 $\text{NaFe}_{1/2}\text{Co}_{1/2}\text{O}_2$ after 50 cycles for a 30 C rate (7.23 A/g) in
92 the voltage range, 2.5–4 V.¹³

93 Here, we report variable-rate discharge cycling studies on P2-
94 $\text{Na}_{0.67}\text{Mn}_{0.8}\text{Mg}_{0.2}\text{O}_2$ electrodes. Galvanostatic measurements
95 coupled with *in situ* and *ex situ* X-ray diffraction (XRD) data
96 have been used to demonstrate the effects of the current in the
97 electrochemical performance of this material which, in turn, is
98 intrinsically related to the structural phases observed during
99 cycling.

100 ■ EXPERIMENTAL SECTION

101 Electrochemical performance of $\text{Na}_{0.67}\text{Mn}_{0.8}\text{Mg}_{0.2}\text{O}_2$ has been
102 evaluated using CR2032 coin cells. Electrode active materials were
103 mixed with carbon black as conductive agent and polyvinylidene
104 fluoride (PVDF) binder in a 80:10:10 ratio. The slurry of the
105 composite was made using *N*-methylpyrrolidone (NMP), and then,
106 the mixture was coated on aluminum foil which acts as current
107 collector. Coated aluminum foils were dried at 120 °C for 2 h in a
108 vacuum oven. Electrodes of 12 mm diameter were punched out of the
109 coated foil and pressed under a load of 4 tons. After pressing the
110 electrodes, these were again dried in a vacuum oven at 120 °C for 2 h.
111 1 M NaPF₆ in ethylene carbonate and propyl carbonate (EC/PC, 1:1
112 vol %) was used as electrolyte, and sodium metal was used as reference
113 electrode. Galvanostatic cycling was performed in the voltage region of
114 1.5–4 V on a Maccor battery tester. Charging of all samples was
115 performed at 12 mA/g, and discharging was performed at different
116 rates, viz., 100, 200, and 400 mA/g. Initially, variable electrode loading
117 was used (e.g., 1.1, 3.2, and 1.1 mg for 100, 200, and 400 mA/g
118 discharge rates, respectively; see Figures S1 and S2); however, for
119 better comparison between applied current rates, electrode loadings
120 were kept consistent at 4.3 ± 0.5 mg. Extended galvanostatic cycling
121 for 100 charge/discharge cycles was undertaken with the above
122 discharge rates, and cells were opened in the discharged state (i.e.,
123 ~1.5 V) at the end of 100 cycles. Electrode loadings for these
124 at the 100 and 400 mA/g discharge rate were 1.1 and 3.2 mg for
125 mA/g discharge rate. Coated Al foils were washed with electrolyte
126 solvent and dried inside the glovebox. Al foils with electrode were
127 mounted on the sample holder and covered with the Kapton foil

before collecting XRD data. XRD data were collected using Cu $K\alpha$ 128
radiation on a Bruker D8 Advance X-ray diffractometer equipped with 129
a LYNXEYE detector. The discharged state of electrodes extracted 130
from *in situ* cells (see below) at the charge rate of 12 mA/g and 131
discharge rates of 100 and 200 mA/g were collected using a 132
PANalytical Empyrean diffractometer with Cu $K\alpha$ radiation. Electro- 133
des were mounted in an airtight dome sample holder inside the 134
glovebox and transferred to the instrument. Two 0.5 (vertical) and 135
4 $x \leq 0.5$ (vertical) mm incoming X-ray slits were used for this 136
experiment, and further details are presented in the Discussion section 137
of this work. 138

An alternative method to prepare samples for *ex situ* diffraction 139
measurements on the first charge/discharge was used to increase the 140
quantity of the active material in the X-ray beam and thus improve 141
XRD signal. Pellets of active material, super S carbon, and Kynar Flex 142
2801 (a copolymer based on PVDF) binder in a mass ratio of 75:18:7 143
were used, and after cycling, the electrodes were washed and dried in a 144
similar manner to the coated electrodes. The extracted powders were 145
then transferred to 0.5 mm glass capillaries. *Ex situ* powder XRD 146
measurements for the first cycle were performed on a Stoe STADI/P 147
diffractometer operating in capillary mode, with Fe $K\alpha_1$ radiation ($\lambda =$ 148
1.936 Å), and data were collected overnight. Rietveld refinements of 149
the structural models and XRD data were carried out using the 150
program Topas Academic.¹⁴ 151

The positive electrodes for *in situ* measurements were manufactured 152
by mixing 80% wt. $\text{Na}_{0.67}\text{Mn}_{0.8}\text{Mg}_{0.2}\text{O}_2$ active material, 10% wt. 153
conductive carbon (Super C65), and 10% wt. PVDF. A few mL of 154
NMP were added, and the resulting slurry was stirred for 1 h. This 155
slurry was then coated on an aluminum foil using similar techniques to 156
that described above. Coin cells with 3 mm diameter holes in the 157
casing and 5 mm diameter holes in the stainless spacer were used for 158
the construction of the coin cells for the *in situ* measurements. The 159
coin cells contained Na metal (~1 mm thickness), glass fiber separator 160
with 1 M NaClO₄ in EC/PC (1:1 wt %) electrolyte solution. *In situ* 161
synchrotron X-ray diffraction experiments were performed within 1–2 162
days after cell construction. Further details regarding coin cell 163
construction and beamline setup can be found in refs 15–20. 164

For the electrochemical tests in coin cells, the electrode loadings 165
were kept consistent at 4.3 ± 0.5 mg for the discharging rates of 100, 166
200, and 400 mAh/g. It is worthwhile to note that NaClO₄ electrolyte 167
can be dangerous as it is sensitive to shocks, and for the development 168
of commercial batteries, an alternative electrolyte is preferable. Note 169
that following the drying step under vacuum, the samples were 170
minimally exposed to air (<1 min) if at all. If transportation of samples 171
or electrodes was required, they were transported in inert conditions 172
and further dried under vacuum prior to cell construction. This was to 173
avoid CO₂ and moisture uptake into these samples as recently 174
evidenced.²¹ 175

In situ synchrotron XRD data were collected on the Powder 176
Diffraction beamline²² at the Australian Synchrotron with a λ of 177
0.68954(2) Å, determined using the NIST 660b LaB₆ standard 178
reference material. Data were collected continuously in 4.4 min 179
acquisitions on the coin cell in transmission geometry throughout the 180
charge/discharge cycles. The coin cells were first charged to 4 V at 12 181
mA/g, then discharged to 1.5 V at 100 mA/g, and charged again to 4 V 182
at 12 mA/g. This corresponds to 0.1–0.2 C on charge and ~1 C on 183
discharge, and the electrode loading was 3 mg. Rietveld refinements 184
were carried out using the GSAS²³ software suite with the EXPGUI²⁴ 185
software interface. 186

187 ■ RESULTS AND DISCUSSION

**Electrochemical Performance of $\text{Na}_{0.67}\text{Mg}_{0.2}\text{Mn}_{0.8}\text{O}_2$ at 188
Different Rates of Discharge.** Galvanostatic charge/ 189
discharge curves of the samples at various discharge rates are 190
shown in Figure 1. During the first charge, which corresponds to 191
the extraction of sodium from $\text{Na}_{0.67}\text{Mg}_{0.2}\text{Mn}_{0.8}\text{O}_2$, the 192
 $\text{Mn}^{3+}/\text{Mn}^{4+}$ oxidation process leads to a charging capacity of 193
~35 mAh/g. During the first discharge, which corresponds to 194
sodium insertion into $\text{Na}_x\text{Mg}_{0.2}\text{Mn}_{0.8}\text{O}_2$, due to the presence of 195

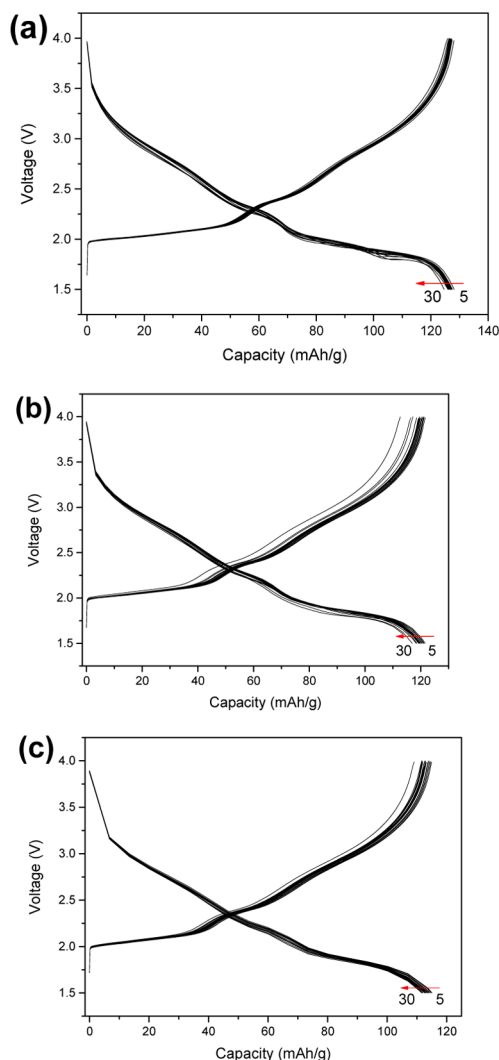


Figure 1. Potential profiles of the $\text{Na}_{0.67}\text{Mn}_{0.8}\text{Mg}_{0.2}\text{O}_2$ electrode charged at 12 mA/g and discharged at (a) 100, (b) 200, and (c) 400 mA/g. Profiles from the 5th to 30th cycles are shown.

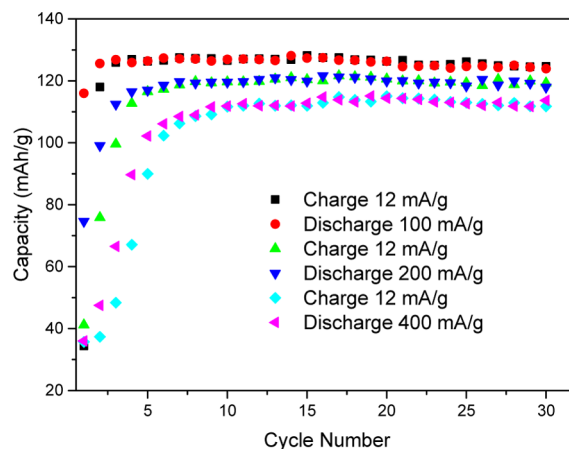


Figure 2. Capacity retention at 12 mA/g charge and 100, 200, and 400 mA/g discharge rates for electrode loading of 4.3 ± 0.5 mg.

performance and cannot be completely neglected. It is interesting to note that one series of cells appeared to show optimal performance at the 200 mA/g discharge rate; however, on further analysis, this appeared to be a result of the electrode loading (see Figures S1 and S2). In any case, in order to understand the mechanisms responsible for the current-rate dependent behavior, we have analyzed the samples by *ex situ* X-ray diffraction (XRD) after 1 and 100 cycles in the fully discharged state at different rates and *in situ* XRD with 12 mA/g charge and 100 mA/g discharge. The *ex situ* data essentially represent extracted data after charge/discharge cycling while the *in situ* data represent the optimal conditions found from the electrochemical results, Figures 1 and 2.

Ex Situ Structural Analysis. XRD data were obtained from samples extracted at various points on the first charge–discharge cycle at a rate of 10 mA/g. Rietveld refinement of structural models with the data from all points on the first charge revealed that the hexagonal P2 structure (space group $P6_3/mmc$) was maintained to full charge, with no formation of the OP4 phase which is observed for lower Mg contents.⁹ A smooth contraction in Mn(Mg)–O bond lengths was observed on sodium extraction accompanying a contraction in a and expansion in c lattice parameters. The plateau around 2 V on discharge is associated with a transition to an orthorhombic phase (space group $Cmcm$). A profile fit is shown in Figure 3, and refined parameters are given in Table 1. It should be noted

the sodium metal as the source of the sodium ions, a greater amount of sodium ions is inserted into the structure compared to the amount extracted during first charge. This leads to high discharge/charge capacities on the second cycle and subsequent cycling. Interestingly, independent of the discharge rate, a large voltage plateau was observed below 2.0 V that contributes significantly to the total capacity.

Cycling performance of the material at different rates of discharge is shown in Figure 2 with two different electrode loadings. Samples were discharged at 100 (low), 200 (moderate), and 400 mA/g (high) rates. Comparing the rates of discharge, the measured capacity from the highest to lowest follows 100 mA/g > 200 mA/g > 400 mA/g using both electrode loads. After 30 cycles at the 4.3 ± 0.5 mg electrode loading, the capacity using discharge rates of 100, 200, and 400 mA/g was 125, 120, and 114 mAh/g, respectively. The observed capacities at these discharge rates are similar which suggests changes when increasing applied discharge rate.

The data presented here are from reproducible cells with very similar electrode loading. We note, however, that there is variation during cell construction (e.g., calendering of the foils and loading density) which does impact electrochemical

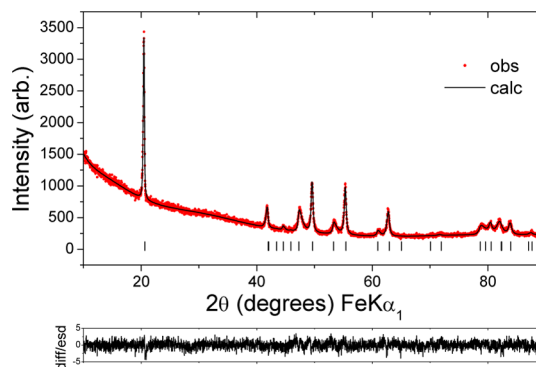


Figure 3. Fitted powder XRD pattern for $\text{Na}_{0.92(1)}\text{Mn}_{0.8}\text{Mg}_{0.2}\text{O}_2$ at the end of discharge. Dots represent the observed data, and the solid line is the calculated pattern. The lower line is the difference/esd. Tick marks indicate the allowed reflections.

Table 1. Refined Crystallographic Parameters for $\text{Na}_{0.92}\text{Mn}_{0.8}\text{Mg}_{0.2}\text{O}_2^a$

| atom | Wyckoff symbol | x/a | y/b | z/c | SOF | B_{iso} |
|---------|----------------|-------|----------|------------|----------|------------------|
| Na1 | 4c | 0 | 0.310(2) | 0.25 | 0.86(1) | 1.2(–) |
| Na2 | 4c | 0 | 0 | 0.25 | 0.055(8) | 1.2(–) |
| Mn1/Mg1 | 4a | 0 | 0 | 0 | 0.8/0.2 | 0.5(–) |
| O1 | 8f | 0 | 0.655(2) | 0.0907(10) | 1 | 0.6(–) |

^aspace group $Cmcm$. $a = 2.8944(6)$ Å, $b = 5.3928(10)$ Å, $c = 10.801(3)$ Å, $R_{\text{wp}} = 4.80\%$, $R_e = 4.54\%$, $R_p = 3.69\%$.

that the magnitude of the orthorhombic distortion at the end of discharge is significantly smaller than that observed for lower Mg contents.⁹ In addition, the Mn(Mg)–O bond lengths show a smaller Jahn–Teller distortion with apical bond lengths of 2.102(11) Å and in-plane distances of 1.938(8) Å, compared to 2.345(3) and 1.936(2) Å for 5% Mg.

The key aspect the first cycle illustrated was the formation of the orthorhombic $Cmcm$ phase at 2 V (Table 1 and Figure 3). To observe the discharged products in more detail, cells were cycled 100 times and extracted at the end of discharge. Initial comparison of the 002 type reflections as a function of discharge rate shows obvious split reflections in the case of the sample discharged at 100 mA/g while higher rates of discharge, 200 and 400 mA/g, do not show obvious splitting (Figure 4a). Rietveld analysis was used to model the phases, and the fit to the data obtained from the sample discharged at 100 mA/g is shown in Figure 4b with further structural details presented in Table 2. The amount of the $Cmcm$ phase that forms at the end of discharge decreases as the current rate is increased, with the cell discharged at 400 mA/g showing a wholly $P6_3/mmc$ electrode. Therefore, there appears to be a current-dependent formation of the $Cmcm$ phase at the end of discharge with slower current rates favoring the formation of this phase, while higher current rates show a predominant $P6_3/mmc$ phase.

In addition to the phase fractions and lattice parameters presented in Table 2, refinements were performed to approximate the sodium content in the respective phases. Na content was found to increase from 0.68 to 0.75 in the $P6_3/mmc$ phase obtained after discharging at 400 mA/g to discharging at 200 mA/g. This corresponds to the greater capacity observed during cycling for discharge at 200 mA/g compared to 400 mA/g.

Correlating the current-dependent formation of the $Cmcm$ phase (Figure 4) to the observed current-dependent electrochemical behavior (Figure 1), it appears that the formation of a significant amount of the $Cmcm$ phase at the end of discharge at 100 mA/g is desirable for the performance of these electrodes. Electrochemically, there is insufficient charge transfer at the 200 and 400 mA/g rates to capture or extract the entire charge/discharge capacity of the battery. At the discharge rates of 100 and 200 mA/g, there exists a mix of $Cmcm$ and $P6_3/mmc$ phases, but the electrode would have sufficient time to relax or phase separate during extraction and subsequent XRD data analysis; therefore, *in situ* XRD was used to study the real-time behavior of the electrode to determine the precise structural evolution of the electrode at the 100 mA/g discharge rate.

In Situ Synchrotron XRD Structural Analysis at 100 mA/g Discharge. Initial Structural Characterization. The cathode in the coin cell adopts a layered structure in the hexagonal space group $P6_3/mmc$ symmetry; a P2-type structure²⁵ and the reported structural model^{8,10} were used as a starting point for analysis. No evidence of CO_2 or water uptake²¹ was found with the collected data. Other models, e.g., O_3 , were tried but the P2-type structure gave the best fit.

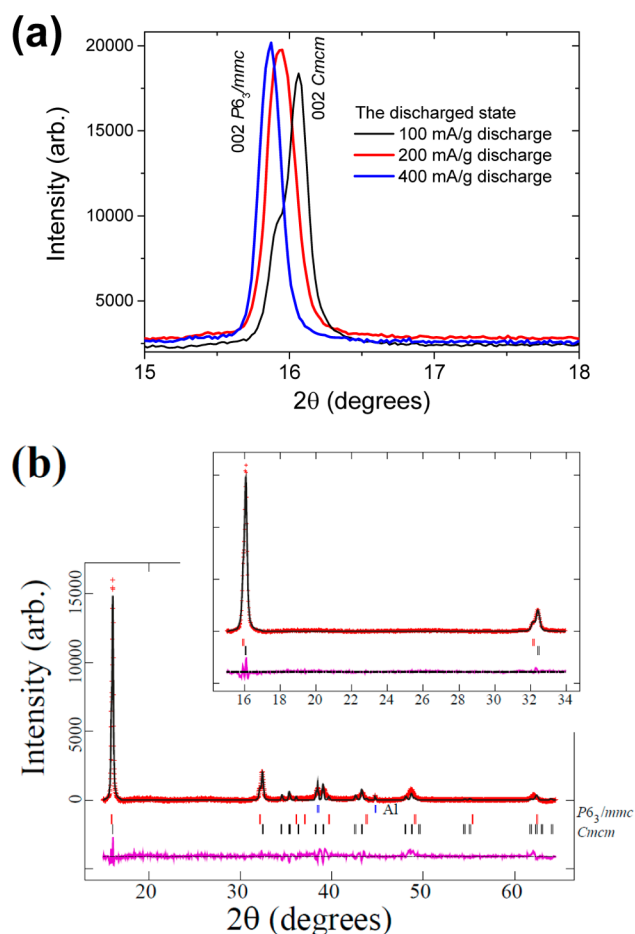


Figure 4. (a) The evolution of the 002 type reflection of extracted electrodes at different discharge rates after 100 cycles of charge/discharge. The two phase behavior is clearly evident during the 100 mA/g discharge while it is predominantly single phase for higher discharging rates. (b) Rietveld refined fit of the $P6_3/mmc$ and $Cmcm$ models and Al to the *ex situ* XRD data set of the 100 mA/g discharged sample. Data are shown as crosses, the calculated Rietveld model as a line through the data, and the difference between the data and the model as the line below the data. The vertical reflection markers are for the phases labeled. The inset in (b) shows the fit to two structural models.

Reflections arising from the aluminum current collector and 298 sodium anode were excluded as their positions did not overlap 299 with many cathode reflections. The background, scale, and 300 lattice parameters were refined initially, and the Mg/Mn site 301 was modeled with 0.2/0.8 occupation. Two Na sites were 302 present Na(1) with $x = y = 0$ and $z = 1/4$ and Na(2) with $x = 303$ $1/3$, $y = 2/3$, and $z = 3/4$, and Na(1) shows lower occupancy 304 than the Na(2) site. Atomic parameters were refined, starting 305 with independently refined atomic displacement parameters 306 (ADPs), oxygen z positional parameter, and sodium site 307 occupancy factors (SOFs). Note, sodium ADPs and SOFs were 308

Table 2. Comparative Parameters from the Structural Analysis of Extracted Electrodes from the Discharged State Using Different Current Rates

| extracted from | phase fraction $Cmcm: P6_3/mmc$ | lattice parameters $Cmcm$ | | | lattice parameters $P6_3/mmc$ | |
|----------------|---------------------------------|---------------------------|-----------|------------|-------------------------------|------------|
| | | <i>a</i> | <i>b</i> | <i>c</i> | <i>a</i> | <i>c</i> |
| 12/100 mA/g | 3.7(3):1 | 2.9081(4) | 5.1848(9) | 11.0354(7) | 2.8726(9) | 11.135(2) |
| 12/200 mA/g | 0.34(2):1 | 2.9080(5) | 5.2336(7) | 11.078(1) | 2.9136(5) | 11.1370(8) |
| 12/400 mA/g | 0.002(2):1 all $P6_3/mmc$ | | | | 2.9177(3) | 11.1690(4) |

not simultaneously refined; SOFs were refined and fixed, and then, the ADPs refined and fixed and so on. In conjunction, profile terms were refined. The structural model fitted well with the data but showed a large mismatch in the 100, 110, and 103 reflections. Fourier maps were used to illustrate what could cause these mismatches. The difference Fourier map (observed – calculated) is shown in Figure 5a,b; in this case, the Na sites

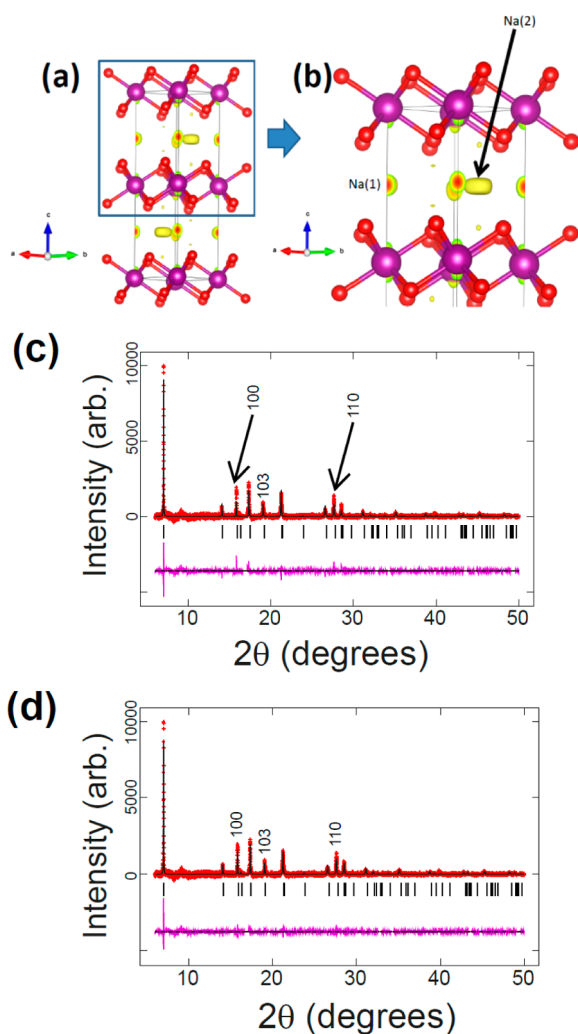


Figure 5. (a, b) The crystal structure of the cathode at OCP with Fourier intensity illustrated when the Na occupancy is set to zero. Mn/Mg is purple, oxygen is red, Fourier intensity is yellow, and the sites are labeled. Rietveld refined fit of the structural model to the initial *in situ* synchrotron XRD data set (c) without and (d) with a preferred orientation term. Data are shown as crosses, the calculated Rietveld model as a line through the data, and the difference between the data and the model as the line below the data. The vertical reflection markers are for $P2\text{-Na}_{0.67}\text{Mn}_{0.8}\text{Mg}_{0.2}\text{O}_2$ and the arrows indicate in (c) the 100 and 110 reflections.

were set to 0, and the positive Fourier density is shown. There appears to be Fourier density around the Mn/Mg site and at the Na(1) and Na(2) sites, further confirming the P2 structure. Interestingly, the Fourier density on the Na(2) site has a distinct nonspherical shape suggesting that this site should be modeled using anisotropic ADPs or reflecting the disordered nature of this site.²⁶ The inclusion of a preferred orientation term along the 100 axis (0.719(4)) improves the fit (see Figure 5c,d), lowers the Na content on both sites to unrealistic values (Na(1) = 0.162(5) and Na(2) = 0.216(8)), and pushes the oxygen positional parameter to a very low value of $z = 0.0704(5)$ but has little influence on the other parameters. The final refined lattice and atomic parameters based on the fits without the preferred orientation term (Figure 5c) are shown in Table 3.

Table 3. Refined Crystallographic Parameters for $\text{Na}_{0.64(1)}\text{Mn}_{0.8}\text{Mg}_{0.2}\text{O}_2$

| atom | Wyckoff | <i>x</i> | <i>y</i> | <i>Z</i> | SOF | isotropic ADP ($\times 100$)/Å ² |
|-------|---------|----------|----------|-----------|----------|---|
| Na(1) | 2 | 0 | 0 | 0.25 | 0.240(6) | 1.08 ^a |
| Na(2) | 2 | 1/3 | 2/3 | 0.75 | 0.40(1) | 6.00 ^{a,b} |
| Mn(1) | 2 | 0 | 0 | 0 | 0.8 | 0.34 ^{a,c} |
| Mg(1) | 2 | 0 | 0 | 0 | 0.2 | 0.34 ^{a,c} |
| O(1) | 4 | 1/3 | 2/3 | 0.0803(5) | 1 | 1.40 ^a |

^aRefined alternatively to SOFs and refined and fixed. ^bCan be modeled anisotropically as 2.01, 1.00, 0.0, 2.01, 0.0, 13.9. ^cConstrained to be equal. Space group = $P6_3/mmc$, in Figure 5c, without preferred orientation 34 refinement parameters, $\chi^2 = 1.63$, $R_p = 2.57\%$, $wRp = 3.78\%$, $a = 2.8717(1)$, $c = 11.1811(2)$ Å.

Phase Evolution. The phase evolution during charge/discharge/charge is predominantly solid solution with a small two-phase region or plateau (orange shading) as shown in Figure 6 for the 002 and 110 reflections. On visual inspection, the electrode does not phase separate (e.g., both $P6_3/mmc$ and $Cmcm$ orthorhombic phases existing or transforming between each other) on discharge. During the solid solution regions, the changes in the 2θ -value of the 002 reflection are opposite to the changes in 110 reflection; e.g., as the 002 2θ -value increases, the 110 2θ -value decreases. This suggests an anisotropic evolution of the lattice parameters within this Na composition.

It is interesting to note that the Mg/Mn ordering observed by Yabuuchi et al.¹⁰ is observed in these data by the 1/3,1/3,0 reflection. This ordering is persistent throughout the charge/discharge cycles (Figure 6c) suggesting that the Mg/Mn ordering does not change during cycling. Additionally, this ordering is observed in the first and second phase (discussed below). Note this reflection sits directly above the amorphous feature due to carbon black and PVDF in the electrode mix which reduces its signal-to-noise ratio.

Taking a closer look at the two-phase region, using stacked plots (Figure 7), the relative similarity of the two-phases

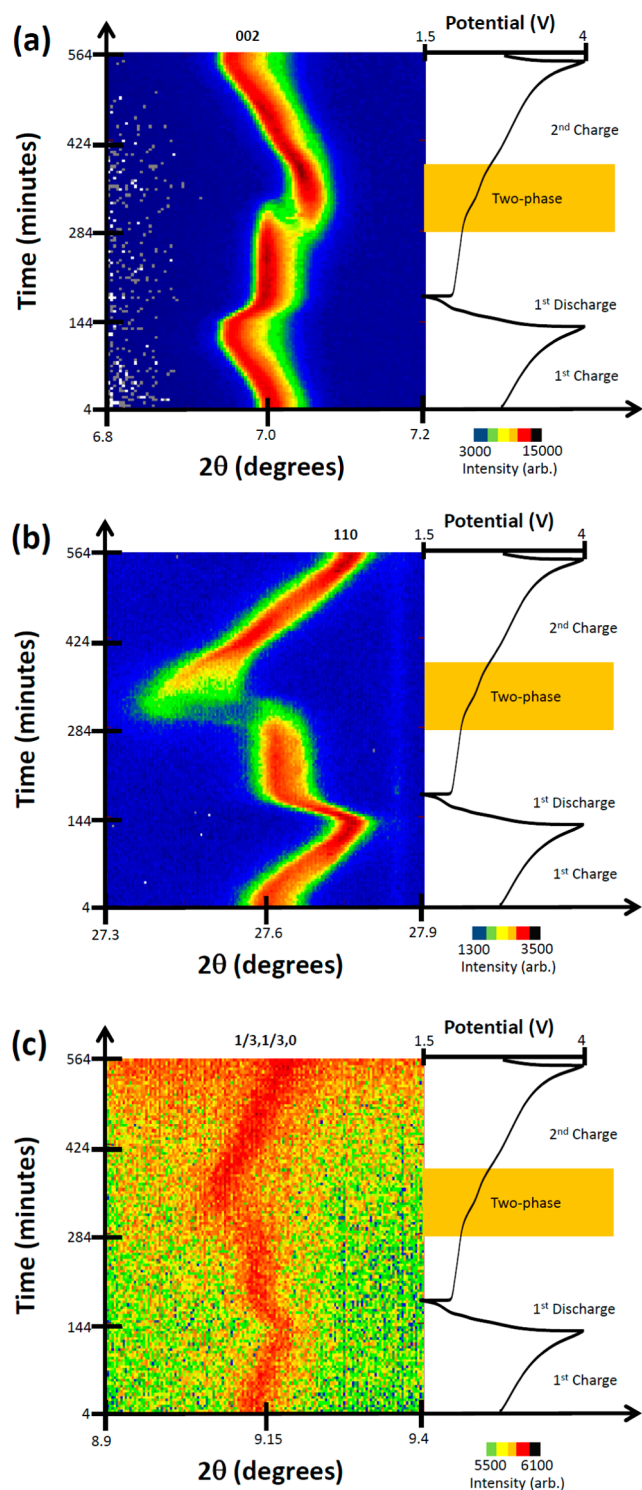


Figure 6. Selected 2θ regions of *in situ* synchrotron XRD data highlighting the evolution of the (a) 002, (b) 110, and (c) $1/3,1/3,0$ (Mn/Mg ordering¹⁰) reflections by a color scale and the potential profile (right). The orange shaded box highlights the two-phase region showing the disappearance and appearance of reflections.

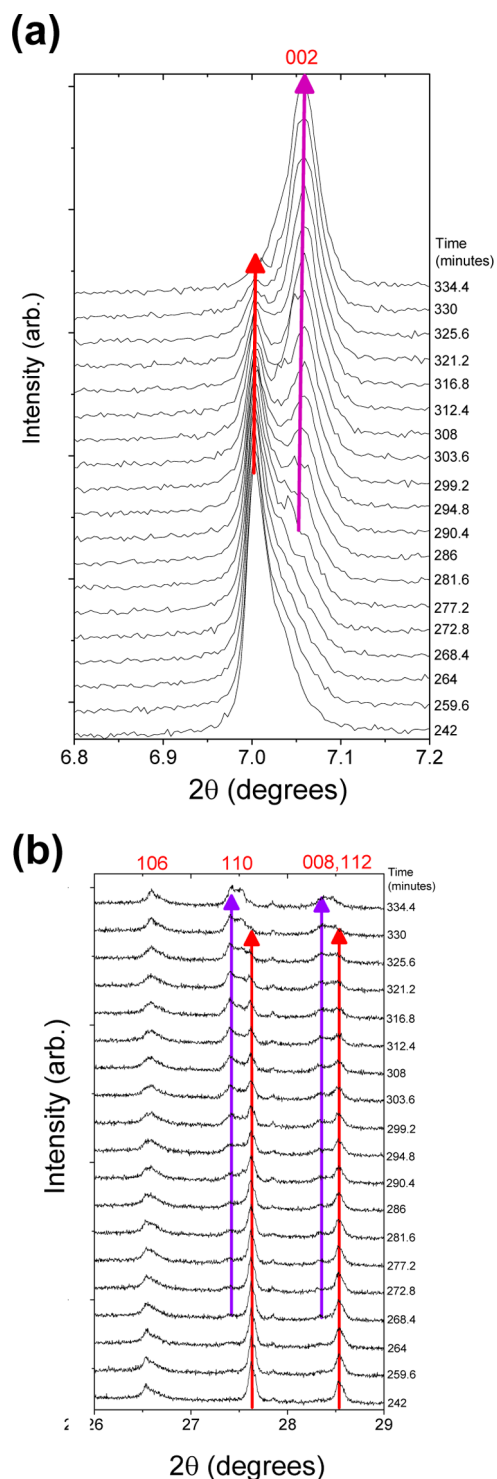


Figure 7. Snapshots via a stacked plot of the *in situ* data of the (a) 002 and (b) 106, 110, and 008, 112 reflections with time shown on the right-hand side of each graph. The red arrows indicate the disappearance of reflections from initial phase (phase 1), and the purple reflections are the new reflections which show subtle changes in the 2θ -value during the same region.

353 becomes more apparent. The two-phases adopt the same
 354 symmetry, and feature only subtle differences in the atomic
 355 parameters, predominantly sodium content similar to findings
 356 for LiCoO_2 ^{27,28} and $\text{Na}_{3-y}\text{V}_2\text{O}_2(\text{PO}_4)_2\text{F}$ ^{18,19} where two-phase
 357 regions are characterized by Na/Li-rich and Na/Li-poor phases.
 358 Note the first phase disappears with minimal change in 2θ -value

(or lattice parameters; see red arrow in Figure 7) while the
 359 second phase appears and shows a small change in 2θ -value
 360 (see purple arrow in Figure 7) during the two-phase region.
 361 The change in 2θ -value is minute but suggests a simultaneous
 362 presence of multiple phase transitions, two-phase and solid
 363

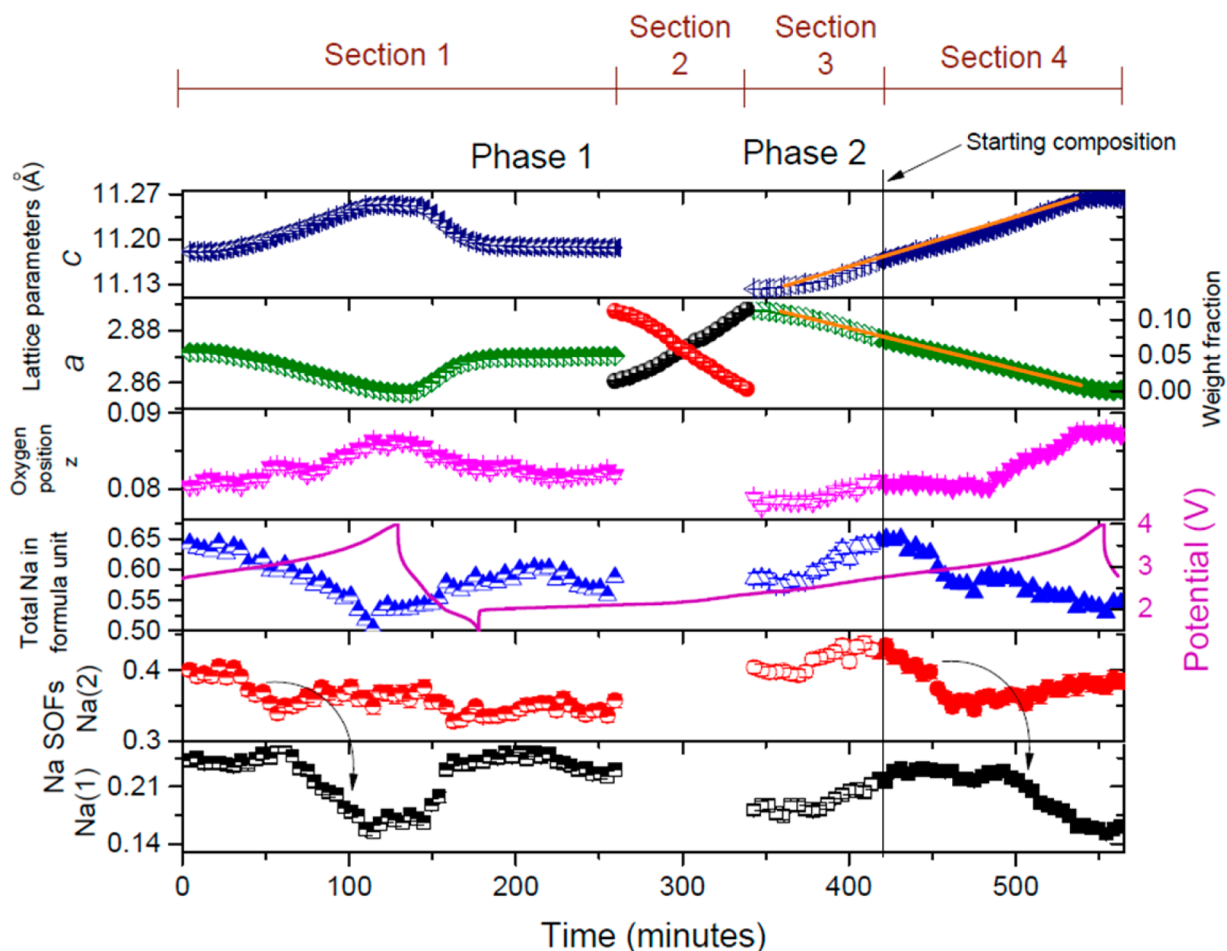


Figure 8. Evolution of the lattice parameters a and c in olive diamonds and blue triangles, respectively; the phase fractions of the initial or 1st phase and the 2nd phase in red and black balls, respectively; the oxygen positional parameters in magenta triangles; the total sodium content in the formula unit in blue triangles; the Na SOFs of the Na(1) and Na(2) sites in black squares and red circles, respectively; the potential profile in purple. Half-filled symbols represent section 1 which encompasses the charge from OCP, discharge, and initial 2nd charge process. The two phase region shown by only the black and red balls are considered as section 2. The section following the two-phase section is section 3 where the 2nd phase evolves in a rather anomalous fashion with respect to the sodium parameters, and this section features open symbols. The final section, section 4, features filled symbols and begins from the composition and voltage that is equivalent to the OCP composition and voltage, as indicated by the straight line.

364 solution, similar to that observed recently by *in situ* neutron
 365 powder diffraction experiments with LiFePO_4 cathodes.²⁹ Note
 366 the simultaneous phase transition region is very small in this
 367 cathode.

368 **Detailed Structural Evolution during Battery Function.** For
 369 the sequential refinements, 4 sections were defined. The first
 370 section until the two-phase reaction begins (half-filled symbols
 371 in Figure 8) corresponds to charge, discharge, and part of the
 372 subsequent charge; the second section is the two-phase region
 373 (spheres in Figure 8); the third section leads up to the original
 374 $\text{Na}_{0.67}\text{Mn}_{0.8}\text{Mg}_{0.2}\text{O}_2$ composition on the second charge (open
 375 symbols in Figure 8); the last section is the remainder of charge
 376 (closed symbols in Figure 8).

377 During first charge, a contracts while c expands until near the
 378 charged state where both a and c begin to stabilize around $a =$
 379 $2.8563(1)$ and $c = 11.2528(3)$ Å. During the fast discharge, a
 380 expands while c contracts and then stabilizes with $a \sim 2.87$ and
 381 $c \sim 11.18$ Å and minimal change is observed during the initial
 382 stages of second charge. This leads to the two-phase region
 383 (discussed below). At the end of the two-phase region, a and c
 384 are at their highest and lowest values, respectively, higher and
 385 lower than the original cathode and after discharging. Here, a is

2.8879(1) and c is 11.1233(2) Å and the potential is 2.36 V. 386
 From this point on, a contracts while c expands during the 387
 remainder of charge. Notably, the contraction of a appears to be 388
 slightly more linear than the expansion of c as highlighted by 389
 the straight lines in Figure 8. This may be intricately tied to the 390
 evolution of the sodium atomic parameters. The original 391
 composition of the cathode returns close to the open circuit 392
 potential (OCP) at 2.72 V (compared below). Interestingly, the 393
 charged cathode on the second charge resembles the charged 394
 electrode on the first charge remarkably well suggesting robust 395
 and repeatable structural transitions during these processes. 396

On charge, the Na content drops from 0.64(1) at OCP to 397
 0.50(1) near the first charged state, corresponding to a change 398
 in Na content of the order of ~ 0.15 . The electrochemically 399
 derived capacity for charge was 30 mAh g^{-1} which corresponds 400
 to a slightly lower change in Na content of ~ 0.14 Na. However, 401
 taking into account surface reactions and noting that the 402
 refinement was a constrained refinement, the values give a good 403
 indication of the evolution. Interestingly, the first 60 min of 404
 charge at 12 mA/g from OCP results in most of the sodium 405
 extraction occurring from the Na(2) site, which is then 406
 “transferred” to the Na(1) site for the remainder of charge as 407

indicated by the arrow in Figure 8. On the fast discharge, the sodium insertion occurs solely on the Na(1) site and the Na(2) occupancy remains the same. This suggests that sodium extraction occurs first from the Na(2) followed by the Na(1) site, while insertion occurs first to the Na(1) site. This shows that the Na(1) site has Na extracted from and inserted into near the charged state. However, sodium does not reinsert or transfer to the Na(2) site on charge. Even on subsequent charge, the Na(2) site remains fairly constant. Thus, Na(1) appears to carry the charge in this region (near first charged state, discharge, initial second charge). The inability to extract more sodium from the Na(2) site during the initial part of the second charge may be the reason that the two-phase region is observed. The two-phase region acts to redistribute Na between the two crystallographic sites. This is evidenced after the two-phase region, where the Na occupancy is larger on the Na(2) site and smaller on the Na(1) compared to the beginning of the two-phase region. It appears that there is a need for Na redistribution that instigates the two-phase region. In the two-phase region (section 2), the first phase and a second phase with slightly different lattice parameters and sodium content are active. The a and c lattice parameters and volume are 2.8879(1) and 11.1233(1) Å and 80.343(3) Å³, respectively, at the end of the two-phase region (2nd phase), and at the beginning, they are 2.8702(1) and 11.1869(2) Å and 79.814(3) Å³ (1st phase). Thus, the a lattice parameter expands, while c shrinks and the overall volume increases. The second phase appears to be an expanded version of the initial first phase. Table 4 shows the major differences between the phases.

Table 4. Refined Crystallographic Parameters for Na_{0.582(11)}Mn_{0.8}Mg_{0.2}O₂ before the Onset of the Two-Phase Region and Na_{0.578(11)}Mn_{0.8}Mg_{0.2}O₂ (Bold) After the Two-Phase Region

| atom | Wyckoff | x | y | z | SOF | isotropic ADP ($\times 100$)/Å ² |
|-------|---------|-----|-----|-----------|----------|--|
| Na(1) | 2 | 0 | 0 | 0.25 | 0.228(7) | 1.08 ^a 0.179(6) |
| Na(2) | 2 | 1/3 | 2/3 | 0.75 | 0.354(9) | 6.00 ^{a,b} 0.399(9) |
| Mn(1) | 2 | 0 | 0 | 0 | 0.8 | 0.34 ^{a,c} 0.13^a |
| Mg(1) | 2 | 0 | 0 | 0 | 0.2 | 0.34 ^{a,c} 0.13^{a,c} |
| O(1) | 4 | 1/3 | 2/3 | 0.0816(5) | 1 | 1.40 ^a 1.36^a |

^aRefined alternatively to SOFs and refined and fixed. ^bCan be modeled anisotropically. ^cConstrained to be equal. Prior to two-phase region 34 refinement parameters, $\chi^2 = 1.65$, $R_p = 2.59\%$, $wRp = 3.83\%$, $a = 2.8702(1)$, $c = 11.1869(2)$ Å. After the two-phase region 34 refinement parameters, $\chi^2 = 1.44$, $R_p = 2.43\%$, $wRp = 3.34\%$, $a = 2.8880(1)$, $c = 11.1234(2)$ Å.

The one factor that appears at odds with the charge/discharge profile is the third section which is shown by the open symbols in Figure 8, following the two-phase region. Here, the sodium content on both sites and overall increases, and this occurs during charge where sodium extraction should be occurring. The speculative explanation for this behavior can be that the presence of surface Na layers (following the two-phase region) allow for sodium extraction giving rise to the

change in potential and charge process, while a small proportion of the surface Na equilibrates and locates onto the sites within the structure, increasing the bulk Na content. The c lattice parameter appears to be slightly nonlinear in this region which may provide further insight for future work. Further work is required to rationalize the behavior in this region of the charge process. In any case, following the Na_{0.67}Mn_{0.8}Mg_{0.2}O₂ composition on the second charge (section 4), the behavior observed from OCP to the first charge (section 1) is essentially reproduced.

Comparing the initial phase in the coin cell at the open circuit potential (OCP) at 2.72 V and the structure in the subsequent charge at 2.72 V, there are minimal differences in the structure. Table 5 shows the atomic parameters for the structure at 2.72 V. The differences are minute: a OCP is 2.8717(1) compared to 2.8771(1) Å at the next 2.72 V on charge; c OCP is 11.1812(2) compared to 11.1672(2) Å; volume OCP is 79.854(3) compared to 80.055(3) Å³. The similarities in the structure show its ability to reversibly insert/extract Na, with only a small expansion of a contraction of c noted at the same states of charge.

DISCUSSION

Overall, the structural transitions are reversible, and at the 12 mA/g charge and 100 mA/g discharge, there are single and two phase reactions occurring but the P2-type structure is preserved. At this rate, there is no evidence of the $Cmcm$ phase on discharge via these *in situ* measurements. From the *ex situ* measurements, it was concluded that the lack of the $Cmcm$ phase and preservation of the P2 structure leads to lower capacities of the Na_{2/3}Mn_{0.8}Mg_{0.2}O₂ cathode at 12/200 and 12/400 mA/g compared to 12/100 mA/g rates. However, the lack of the $Cmcm$ phase during *in situ* experiments suggests a minute quantity may form under continuous operation at 12/100 mA/g.

A concern with the coin cell used in this work, containing circular Kapton-tape covered holes to allow X-ray transmission as compared to cells with Be windows or the AMPPIX cell,³⁰ is the potential for a “lag effect” of the electrochemical reaction in the region of the hole. In other words, the XRD pattern is taken of a region that may be behind the true electrochemistry of the cell. In order to test this, *in situ* cells with the Na_{0.67}Mn_{0.8}Mg_{0.2}O₂ electrode were tested offline under two conditions at the 200 mA/g discharge rate. The first cell was discharged to 1.5 V and allowed to rest before another discharge to 1.5 V was applied, and this process was repeated 5 times. The second cell was just discharged to 1.5 V. Both cells were immediately extracted (~15 min, via a quick transfer to the glovebox). XRD data were collected using two slits that control the dimension of the incoming X-ray beam on the sample. The first data set was collected with an incoming slit of 2 $x \leq 0.5$ (vertical) mm dimension which was centered on the central part of the electrode and the second data set with a slit of 4 $x \leq 0.5$ (vertical) mm. The patterns clearly show the presence of a two phase electrode (see Figure S3). For the 100 mA/g discharge rate electrode using this slit configuration, a similar two-phase electrode is observed but with a slightly different phase composition (see Figure S4). The two phase electrode at the 100 and 200 mA/g discharge rate in combination with the *in situ* synchrotron XRD data at the 100 mA/g discharge rate suggest that the process of electrode extraction allows the electrode to relax to a state that is not kinetically state but rather closer to the thermodynamically sta

Table 5. Refined Crystallographic Parameters for $\text{Na}_{0.64(1)}\text{Mn}_{0.8}\text{Mg}_{0.2}\text{O}_2$ at 2.72 V on Second Charge

| atom | Wyckoff | X | y | z | SOF | isotropic ADP ($\times 100$)/ \AA^2 |
|-------|---------|-----|-----|-----------|-----------|--|
| Na(1) | 2 | 0 | 0 | 0.25 | 0.218(6) | 0.53 ^a |
| Na(2) | 2 | 1/3 | 2/3 | 0.75 | 0.421(10) | 6.99 ^{a,b} |
| Mn(1) | 2 | 0 | 0 | 0 | 0.8 | 0.13 ^{a,c} |
| Mg(1) | 2 | 0 | 0 | 0 | 0.2 | 0.13 ^{a,c} |
| O(1) | 4 | 1/3 | 2/3 | 0.0808(5) | 1 | 1.36 ^a |

^aRefined alternatively to SOFs and refined and fixed. ^bCan be modeled anisotropically. ^cConstrained to be equal. Space group = $P6_3/mmc$, 34 refinement parameters, $\chi^2 = 1.69$, $R_p = 2.57\%$, $wRp = 3.90\%$, $a = 2.8771(1)$, $c = 11.1672(2)$ \AA .

508 state with two-phases present. Only slight variations in peak
509 intensity are found between the 2 and 4 mm slits indicating that
510 the regions with the Kapton window does not “lag” significantly
511 behind the majority of the electrode as expected for these
512 materials. In addition, there are significant differences in phase
513 composition (see Figures S3 and S4) between the electrodes
514 that are straightly charged at 100 and 200 mA/g and
515 sequentially discharged, rest-discharged, further illustrating the
516 role electrode relaxation has on the processes under
517 investigation. It is important to note that *in situ* (*operando*)
518 processes can detail kinetic information, while extracting
519 electrodes for *ex situ* studies can result in the convolution of
520 the actual electrode state and any relaxation mechanisms that
521 occur.³¹

522 At 12 mA/g discharge, the material delivers around 150
523 mAh/g⁹ and the *Cmcm* phase is formed at the discharged state.
524 As the discharge current rate is increased, there is an observed
525 capacity loss, as there is less capacity that is extracted from the
526 electrode; thus, less of the *Cmcm* phase is formed at the
527 discharged state. In other words, more of the *Cmcm* phase is
528 formed at the 12 mA/g than the 100 mA/g discharge rate. The
529 loss of capacity is a commonly seen occurrence as current rate
530 is increased.³² Coupling this behavior with the *in situ* XRD data,
531 which shows that the *Cmcm* phase is not formed at the 100
532 mA/g discharge rate under continuous operation in contrast to
533 *Cmcm* formation in *ex situ* studies, suggests reaction kinetics
534 plays a critical role.

535 The question of kinetics near the discharged state remains a
536 complex problem. The rate limiting process and the process
537 that limits capacity can be the nucleation and growth of the
538 *Cmcm* or P2 phase in all the particles (one particle can be P2
539 while another in *Cmcm*) or within particles (e.g., core/shell of
540 P2 and *Cmcm* phases);^{33–35} related to the diffusion of sodium
541 in the P2 and *Cmcm* phases; lattice avoidance of the two phase
542 mechanism;^{29,30} electronic/ionic conductivity of the electrode
543 particle surface and bulk; or combinations of these processes to
544 name a few options. Further work is required to rationalize
545 such intricacies.

546 If one considers the percentage of the *Cmcm* phase formed
547 for the 100, 200, and 400 mA/g discharge, there is a distinct
548 reduction in quantity from ~ 78 and 25 to less than 0.2%,
549 respectively (see Table 2 for ratios), *via ex situ* data after 100
550 cycles. Factoring in the *in situ* data collected at a discharge rate
551 of 100 mA/g with no evidence of the *Cmcm* phase, the most
552 likely cause of the formation of the *Cmcm* phase at 100 and 200
553 mA/g is electrode relaxation and extraction. On the basis of this
554 information and the recorded capacity at 400 mA/g, it is
555 reasonable to suggest that the electrode does not reach the state
556 of charge required where the *Cmcm* phase can form, and thus,
557 any electrode relaxation will result in the P2 phase being
558 maintained at 400 mA/g.

Sodium extraction (and insertion) often results in phase
559 transitions, some dramatic and some minimal, during battery
560 charge (or discharge) in this family of layered com-
561 pounds.^{13,17,36} Typically, as the current rate is increased, the
562 amount of sodium extracted (or inserted) decreases which
563 corresponds to a lower measured energy density or capacity.
564 During the charge process in $\text{Na}_{0.67}\text{Mn}_{0.8}\text{Mg}_{0.2}\text{O}_2$, there is a
565 phase transition between two P2-type or hexagonal $P6_3/mmc$
566 phases and this results in minimal structural change. In contrast,
567 the hexagonal $P6_3/mmc$ to orthorhombic *Cmcm* phase
568 transition near the discharged state appears to be one of the
569 most significant factors that influence capacity and the largest
570 structural change exhibited by this electrode. These phases are
571 often referred to as P2 and P'2, respectively, and are also
572 observed in other P2-type electrodes.^{13,36} The details of the
573 hexagonal $P6_3/mmc$ to orthorhombic *Cmcm* transition are
574 elegantly detailed in ref 36 which shows that with increasing
575 Jahn–Teller active Mn^{3+} a cooperative distortion occurs that
576 promotes this phase transition. Similar to the work on the
577 $\text{Na}_x\text{Fe}_{0.5}\text{Mn}_{0.5}\text{O}_2$, there appears to be a two-phase mixture at
578 the end of discharge *via ex situ* measurements,³⁶ but our *in situ*
579 and *ex situ* findings suggest that this is a rate dependent reaction
580 which does not occur at higher applied discharge rates. 581

CONCLUSIONS

582 The discharge current rate can influence the electrochemical
583 performance of electrodes, and there is a structural reason
584 attributable to this in the case of $\text{Na}_{0.67}\text{Mn}_{0.8}\text{Mg}_{0.2}\text{O}_2$ electrodes.
585 The transition of the $P6_3/mmc$ to the *Cmcm* phase at the
586 discharged state is in part responsible for the marginally
587 superior electrochemical performance with a discharge rate of
588 100 mA/g compared to the discharge rates of 200 and 400 mA/
589 g. Although in an *ex situ* experiment, the *Cmcm* phase is clearly
590 present at the discharged state with a 100 mA/g discharge rate;
591 under real cell conditions (e.g., nonequilibrium), the *Cmcm*
592 phase is not formed at the discharged state. The *Cmcm* phase
593 does begin to form if the electrode is extracted from the cell,
594 suggesting that the 100 mA/g discharge rate inhibits the
595 formation of the *Cmcm* phase under continuous cycling
596 conditions. From a chemical point-of-view, the nucleation
597 and growth of the *Cmcm* phase and subsequent removal
598 enhances the capacity of the electrochemical process, e.g.,
599 allowing sodium to be inserted into the *Cmcm* phase and thus
600 increasing capacity. At higher discharge rates of 400 mA/g,
601 there is insufficient utilization of the electrode which can lead to
602 lower capacities compared to the 100 and 200 mA/g discharge
603 rate. Therefore, the two-phase phase electrode or moving
604 toward a two-phase electrode at the discharged state appears to
605 be a prerequisite for better cycling performance. The current-
606 rate dependent performance is intricately linked to the
607 structure of electrodes and characterizing this link will allow
608 researchers and industry to maximize the performance of 609

610 electrode materials. A synergy is required between the
611 electronic controls of current rate during operation and the
612 expected structural-electrochemical performance parameters.

613 ■ ASSOCIATED CONTENT

614 ● Supporting Information

615 The Supporting Information is available free of charge on the
616 ACS Publications website at DOI: 10.1021/acs.chemmater.5b02142.

618 Galvanostatic cycling, capacity versus cycle number of
619 electrodes with different loadings, and *ex situ* XRD
620 analysis of electrodes extracted from coin cells with holes
621 covered by Kapton tape (PDF)

622 ■ AUTHOR INFORMATION

623 Corresponding Authors

624 *Phone: +61 2 93854714. E-mail: Neeraj.sharma@unsw.edu.
625 au.

626 *Phone: +34 945297108. E-mail: trojo@cicenergigune.com.

627 Author Contributions

628 The manuscript was written through contributions of all
629 authors. All authors have given approval to the final version of
630 the manuscript.

631 Notes

632 The authors declare no competing financial interest.

633 ■ ACKNOWLEDGMENTS

634 We would like to thank undergraduate UNSW students Laura
635 Jeffress, Damian Goonetilleke, and Emily Cheung for assistance
636 during the *in situ* synchrotron XRD experiments. J.C.P. would
637 like to thank UNSW/ANSTO for the PhD Scholarship. N.S.
638 would like to thank AINSE Ltd for providing support through
639 the research fellowship scheme. Part of this research was
640 undertaken on the Powder Diffraction beamline at the
641 Australian Synchrotron, Victoria, Australia. CIC Energigune
642 work was financially supported by Ministerio de Economía y
643 Competitividad (Proyecto I+D. Retos 2013), reference
644 numbers ENE 2013-44330-R and FPD1-2013-17329, and the
645 Gobierno Vasco/Eusko Jaurlaritz (Ertorke CIC Energigune 10,
646 SAIOTEK-12 ENERGIBA and IT570-13). P.G.B. is indebted
647 to the EPSRC, including the SUPERGEN programme, for
648 financial support

649 ■ REFERENCES

650 (1) Whittingham, M. S. Chemistry of intercalation compounds:
651 Metal guests in chalcogenide hosts. *Prog. Solid State Chem.* **1978**, *12*,
652 41.
653 (2) Palomares, V.; Serras, P.; Villaluenga, I.; Hueso, K. B.; Carretero-
654 Gonzalez, J.; Rojo, T. Na-ion batteries, recent advances and present
655 challenges to become low cost energy storage systems. *Energy Environ.*
656 *Sci.* **2012**, *5*, 5884.
657 (3) Palomares, V.; Casas-Cabanas, M.; Castillo-Martinez, E.; Han, M.
658 H.; Rojo, T. Update on Na-based battery materials. A growing research
659 path. *Energy Environ. Sci.* **2013**, *6*, 2312.
660 (4) Han, M. H.; Gonzalo, E.; Singh, G.; Rojo, T. A comprehensive
661 review of sodium layered oxides: powerful cathodes for Na-ion
662 batteries. *Energy Environ. Sci.* **2015**, *8*, 81.
663 (5) Delmas, C.; Fouassier, C.; Hagenmuller, P. Structural
664 classification and properties of the layered oxides. *Physica B+C*
665 **1980**, *99*, 81.
666 (6) Yabuuchi, N.; Kajiyama, M.; Iwatate, J.; Nishikawa, H.; Hitomi,
667 S.; Okuyama, R.; Usui, R.; Yamada, Y.; Komaba, S. P2-type

$\text{Na}_x[\text{Fe}_{1/2}\text{Mn}_{1/2}]\text{O}_2$ made from earth-abundant elements for recharge-
able Na batteries. *Nat. Mater.* **2012**, *11*, 512. 669

(7) Paulsen, J. M.; Dahn, J. R. Studies of the layered manganese
670 bronzes, $\text{Na}_{2/3}[\text{Mn}_{1-x}\text{M}_x]\text{O}_2$ with $\text{M} = \text{Co}, \text{Ni}, \text{Li}$, and $\text{Li}_{2/3}[\text{Mn}_{1-x}\text{M}_x]$.
671 O_2 prepared by ion-exchange. *Solid State Ionics* **1999**, *126*, 3. 672

(8) Parant, J.-P.; Olazcuaga, R.; Devalette, M.; Fouassier, C.;
673 Hagenmuller, P. Sur Quelques Nouvelles Phases de Formule
674 Na_xMnO_2 ($x \leq 1$). *J. Solid State Chem.* **1971**, *3*, 1. 675

(9) Billaud, J.; Singh, G.; Armstrong, A. R.; Gonzalo, E.; Roddatis, V.;
676 Armand, M.; Rojo, T.; Bruce, P. G. $\text{Na}_{0.67}\text{Mn}_{1-x}\text{Mg}_x\text{O}_2$ ($0 \leq x \leq 0.2$): a
677 high capacity cathode for sodium-ion batteries. *Energy Environ. Sci.* **2014**, *7*, 1387. 679

(10) Yabuuchi, N.; Hara, R.; Kubota, K.; Paulsen, J.; Kumakura, S.;
680 Komaba, S. New electrode material for rechargeable sodium batteries:
681 P2-type $\text{Na}_{2/3}[\text{Mg}_{0.28}\text{Mn}_{0.72}]\text{O}_2$ with anomalously high reversible
682 capacity. *J. Mater. Chem. A* **2014**, *2*, 16851. 683

(11) Sathiyaa, M.; Ramesha, K.; Rousse, G.; Foix, D.; Gonbeau, D.;
684 Prakash, A. S.; Doublet, M.-L.; Hemalatha, K.; Tarascon, J. M. High
685 Performance $\text{Li}_2\text{Ru}_{1-y}\text{Mn}_y\text{O}_3$ ($0.2 \leq y \leq 0.8$) Cathode Materials for
686 Rechargeable Lithium-Ion Batteries: Their Understanding. *Chem.*
687 *Mater.* **2013**, *25*, 1121. 688

(12) Kim, D.; Kang, S.-H.; Slater, M.; Rood, S.; Vaughey, J. T.; Karan,
689 N.; Balasubramanian, M.; Johnson, C. S. Enabling Sodium Batteries
690 Using Lithium-Substituted Sodium Layered Transition Metal Oxide
691 Cathodes. *Adv. Energy Mater.* **2011**, *1*, 333. 692

(13) Yoshida, H.; Yabuuchi, N.; Komaba, S. $\text{NaFe}_{0.5}\text{Co}_{0.5}\text{O}_2$ as high
693 energy and power positive electrode for Na-ion batteries. *Electrochem.*
694 *Commun.* **2013**, *34*, 60. 695

(14) Coelho, A. A. Whole-profile structure solution from powder
696 diffraction data using simulated annealing. *J. Appl. Crystallogr.* **2000**,
697 *33*, 899. 698

(15) Brant, W. R.; Schmid, S.; Du, G.; Gu, Q.; Sharma, N. A simple
699 electrochemical cell for in-situ fundamental structural analysis using
700 synchrotron X-ray powder diffraction. *J. Power Sources* **2013**, *244*, 109. 701

(16) Gummow, R. J.; Sharma, N.; Feng, R.; Han, G.; He, Y. High
702 Performance Composite Lithium-Rich Nickel Manganese Oxide
703 Cathodes for Lithium-Ion Batteries. *J. Electrochem. Soc.* **2013**, *160*,
704 A1856. 705

(17) Sharma, N.; Gonzalo, E.; Pramudita, J. C.; Han, M. H.; Brand,
706 H. E. A.; Hart, J. N.; Pang, W. K.; Guo, Z.; Rojo, T. The unique
707 structural evolution of the O3-phase $\text{Na}_{2/3}\text{Fe}_{2/3}\text{Mn}_{1/3}\text{O}_2$ during high
708 rate charge/discharge: A sodium-centred perspective. *Adv. Funct.*
709 *Mater.* **2015**, *25*, 4994. 710

(18) Sharma, N.; Serras, P.; Palomares, V.; Brand, H. E. A.; Alonso,
711 J.; Kubiak, P.; Fdez-Gubieda, M. L.; Rojo, T. The sodium distribution
712 and reaction mechanisms of a $\text{Na}_3\text{V}_2\text{O}_7(\text{PO}_4)_2\text{F}$ electrode during use
713 in a sodium-ion battery. *Chem. Mater.* **2014**, *26*, 3391. 714

(19) Serras, P.; Palomares, V.; Rojo, T.; Brand, H. E. A.; Sharma, N.
715 Structural evolution of high energy density $\text{V}^{3+}/\text{V}^{4+}$ mixed valent
716 $\text{Na}_3\text{V}_2\text{O}_{2x}(\text{PO}_4)_{2-2x}\text{F}_{3-2x}$ ($x = 0.8$) sodium vanadium fluorophosphate
717 using in-situ synchrotron X-ray powder diffraction. *J. Mater. Chem. A*
718 **2014**, *2*, 7766. 719

(20) Pramudita, J. C.; Schmid, S.; Godfrey, T.; Whittle, T.; Alam, M.;
720 Hanley, T.; Brand, H. E. A.; Sharma, N. Sodium uptake in cell
721 construction and subsequent in operando electrode behaviour of
722 Prussian Blue Analogues, $\text{Fe}[\text{Fe}(\text{CN})_6]_{1-x}\text{yH}_2\text{O}$ and $\text{FeCo}(\text{CN})_6$.
723 *Phys. Chem. Chem. Phys.* **2014**, *16*, 24178. 724

(21) Duffort, V.; Talaie, E.; Black, R.; Nazar, L. F. Uptake of CO_2 in
725 Layered $\text{P2-Na}_{0.67}\text{Mn}_{0.5}\text{Fe}_{0.5}\text{O}_2$: Insertion of Carbonate Anions. *Chem.*
726 *Mater.* **2015**, *27*, 2515. 727

(22) Wallwork, K. S.; Kennedy, B. J.; Wang, D. The High Resolution
728 Powder Diffraction Beamline for the Australian Synchrotron. *AIP Conf.*
729 *Proc.* **2006**, 879. 730

(23) Larson, A. C.; Von Dreele, R. B.; *Los Alamos National*
731 *Laboratory Report LAUR 86-748*; Los Alamos National Laboratory:
732 Los Alamos, NM, 1994. 733

(24) Toby, B. H. EXPGUI, a graphical user interface for GSAS. *J.*
734 *Appl. Crystallogr.* **2001**, *34*, 210. 735

- 736 (25) Guignard, M.; Didier, C.; Darriet, J.; Bordet, P.; Elkaim, E.;
737 Delmas, C. P2-Na_xVO₂ system as electrodes for batteries and electron-
738 correlated materials. *Nat. Mater.* **2013**, *12*, 74.
- 739 (26) Wang, Y.; Xiao, R.; Hu, Y.-S.; Avdeev, M.; Chen, L. P2-
740 Na_{0.6}[Cr_{0.6}Ti_{0.4}]O₂ cation-disordered electrode for high-rate symmetric
741 rechargeable sodium-ion batteries. *Nat. Commun.* **2015**, *6*, 6954.
- 742 (27) Takahashi, Y.; Kijima, N.; Tokiwa, K.; Watanabe, T.; Akimoto, J.
743 Single-crystal synthesis, structure refinement and electrical properties
744 of Li_{0.3}CoO₂. *J. Phys.: Condens. Matter* **2007**, *19*, 436202.
- 745 (28) Sharma, N.; Peterson, V. K.; Elcombe, M. M.; Avdeev, M.;
746 Studer, A. J.; Blagojevic, N.; Yusoff, R.; Kamarulzaman, N. Structural
747 changes in a commercial lithium ion battery during electrochemical
748 cycling: An *in-situ* neutron diffraction study. *J. Power Sources* **2010**, *195*,
749 8258.
- 750 (29) Sharma, N.; Guo, X.; Du, G.; Guo, Z.; Wang, J.; Wang, Z.;
751 Peterson, V. K. Direct Evidence of Concurrent Solid-Solution and
752 Two-Phase Reactions and the Nonequilibrium Structural Evolution of
753 LiFePO₄. *J. Am. Chem. Soc.* **2012**, *134*, 7867–7873.
- 754 (30) Borkiewicz, O. J.; Shyam, B.; Wiaderek, K. M.; Kurtz, C.;
755 Chupas, P. J.; Chapman, K. W. The AMPIX electrochemical cell: a
756 versatile apparatus for in situ X-ray scattering and spectroscopic
757 measurements. *J. Appl. Crystallogr.* **2012**, *45*, 1261.
- 758 (31) Sharma, N.; Pang, W. K.; Guo, Z.; Peterson, V. K. In Situ
759 Powder Diffraction Studies of Electrode Materials in Rechargeable
760 Batteries. *ChemSusChem* **2015**, *8*, 2826.
- 761 (32) Sharma, N.; Peterson, V. K. Current dependency of lattice
762 fluctuations and phase evolution of electrodes in lithium-ion batteries
763 investigated by in situ neutron diffraction. *Electrochim. Acta* **2013**, *101*,
764 79.
- 765 (33) Orvananos, B.; Yu, H.-C.; Abdellahi, A.; Malik, R.; Grey, C. P.;
766 Ceder, G.; Thornton, K. Kinetics of Nanoparticle Interactions in
767 Battery Electrodes. *J. Electrochem. Soc.* **2015**, *162*, A965.
- 768 (34) Orvananos, B.; Malik, R.; Yu, H.-C.; Abdellahi, A.; Grey, C. P.;
769 Ceder, G.; Thornton, K. Architecture Dependence on the Dynamics of
770 Nano-LiFePO₄ Electrodes. *Electrochim. Acta* **2014**, *137*, 245.
- 771 (35) Bai, P.; Cogswell, D. A.; Bazant, M. Z. Suppression of phase
772 separation in LiFePO₄ nanoparticles during battery discharge. *Nano*
773 *Lett.* **2011**, *11*, 4890.
- 774 (36) Talaie, E.; Duffort, V.; Smith, H. L.; Fultz, B.; Nazar, L. F.
775 Structure of the high voltage phase of layered P2-Na_{2/3-z}[Mn_{1/2}Fe_{1/2}]-
776 O₂ and the positive effect of Ni substitution on its stability†. *Energy*
777 *Environ. Sci.* **2015**, *8*, 2512.